Computer Physics Communications 292 (2023) 108857

Contents lists available at ScienceDirect

Computer Physics Communications

journal homepage: www.elsevier.com/locate/cpc

Computer Programs in Physics

Tuning and interpretation of electronic transport properties with m*2T ☆☆

Luca Bonaldo [a,*], Terry Ethan Stearns [a], Ilaria Siloi [b], Nicholas A. Mecholsky [c], Marco Fornari [a]

[a] Department of Physics and Science of Advanced Materials Program, Central Michigan University, Mt. Pleasant, MI, 48859, United States
[b] Dipartimento di Fisica e Astronomia "G. Galilei", Università degli Studi di Padova, via Marzolo 8, I-35131 Padova, Italy
[c] Department of Physics and Vitreous State Laboratory, The Catholic University, Washington, DC 20064, United States

ARTICLE INFO

Article history:
Received 8 April 2023
Received in revised form 30 June 2023
Accepted 12 July 2023
Available online 25 July 2023

Dataset link: https://github.com/marcofornari/etransport.git

Keywords:
Electrical conductivity
Seebeck coefficient
Carrier concentration
Electronic transport
Effective mass
Thermoelectricity

ABSTRACT

Electronic transport coefficients such as the electrical conductivity, the termo-power, and the charge carrier concentration are routinely measured in a variety of application areas such as electronics or thermoelectric power-generation and cooling. Using fitting procedures, those measurements are used to infer microscopic features of the samples. The code m*2T facilitates the estimation of electronic structure parameters such as the effective masses and band energies improving the current approach by increasing the complexity of the band structure representation. The software is designed with a server-client architecture to enhance performance and scalability. The server is implemented in the Julia programming language. We illustrate the design and the efficiency of the code with selected applications, which are relevant to the optimization of thermoelectric materials.

Program summary

Program Title: m*2T
CPC Library link to program files: https://doi.org/10.17632/494nj6ftbv.1
Developer's repository link: https://github.com/marcofornari/etransport.git
Licensing provisions: GPLv3
Programming language: Julia, Python.
Nature of problem: Electronic transport measurements are routinely used to link the functional properties exploited in electronics and energy sciences applications with the underlying electronic structure of the material under investigation. Experimentalists collect data of derived and integrated physical quantities, from which they estimate properties and parameters, e.g., nature of the conduction mechanisms and effective mass. The interpretation is based on simplistic models that rarely represent the complexity of the band structure. The code m*2T improves the current state of the art and facilitates the estimation of effective masses and energies from experimental measurements of electrical conductivity, Seebeck coefficients, and carrier concentration using a multi-valley anisotropic parabolic band structure as a model for the unknown real band structure. Experimental data can be imported and visualized to facilitate the comparison with theoretical analysis.
Solution method: The Boltzmann equation within the relaxation-time approximation is used to compute the electronic transport tensors from the electronic density of states characterized in terms of a set of effective masses tensors m_i^* and critical energies ϵ_i. Numerical and analytical techniques are adopted to integrate the Boltzmann equation efficiently. By tuning the features of the density of states, temperature, Fermi level, and the functional expression for the relaxation time, the software streamlines the reconstruction of the underlying electronic properties from experimental data.
Additional comments including restrictions and unusual features: The software is designed with a server-client architecture to enhance performance and scalability. The server is implemented in the Julia programming language as a stand-alone library. It performs all the numerical operations to compute the transport tensors from a set of multi-valley parabolic band structures. The client is implemented either

☆ The review of this paper was arranged by Prof. Weigel Martin.
☆☆ This paper and its associated computer program are available via the Computer Physics Communications homepage on ScienceDirect (http://www.sciencedirect.com/science/journal/00104655).

* Corresponding author.
E-mail address: bonal1l@cmich.edu (L. Bonaldo).

https://doi.org/10.1016/j.cpc.2023.108857

as a command-line user interface (CLI) or a graphical user interface (GUI) written in the Python programming language. The communications between the server and clients are handled by a REST API, where the data are exchanged using JSON payloads.

1. Introduction

The effective mass characterizes how freely electrons or holes propagate inside a material and is critical in describing the transport phenomena exploited in the electronic and optoelectronic industry, as well as in photovoltaic and thermoelectric energy harvesting and cooling. Today, various experimental techniques are available to measure the effective mass of a material, e.g., cyclotron resonance [1],[2,3], de Haas-Van Alphen and Shubnikov-de Haas oscillations [4], [5], magnetophonon resonance [6],[5], [7], angle-resolved photo-emission spectroscopy [8], reflectivity and absorption measurements [9], and measurements of electron transport properties [10]; the measured values can vary considerably depending on the experimental method employed [11]. Despite the widespread use, several levels of approximations are always involved when comparing experimental measurements of the effective mass with theoretical predictions. In the case of electronic transport, the effective mass is obtained *indirectly*, assuming simplified or phenomenological models that usually involve a single quadratic energy dispersion for the electrons of the crystal. From a theoretical point of view, the concept of the effective mass was first introduced by L. D. Landau in his Fermi-liquid theory [12]. Under certain conditions, the dynamics of an otherwise intractable strongly interacting many-body quantum system of electrons can be described as a gas of weakly interacting fictitious fermions called *quasiparticles*, with an appropriately renormalized effective mass. If the electrons in the material are modeled as a gas of independent non-interacting quasiparticles moving in a uniform, positively charged background, the effective mass is either the mass term in the kinetic energy or the mass of the rotating quasiparticle in the definition of the cyclotron resonance frequency. Moreover, since the measurements are often performed along a single direction or in a polycrystalline sample, the effective mass is generally assumed to be isotropic.

In electronic structure theory, the effective masses are tensors associated with the critical points: maxima, minima, or saddles of the band structure. Given a band structure, a complicated function $\epsilon_s(\mathbf{k})$ from $R^3 \to R^s$, the Taylor expansion at the quadratic order near selected critical points provides the Hessian matrices. The effective masses are then obtained by computing the inverse of the Hessian in the proximity of the critical points in the Brillouin zone [13]. Several interpolation methods can be used to determine first and second-order derivatives of $\epsilon_s(\mathbf{k})$ and, from those, transport quantities such as the electrical conductivity, σ, the Seebeck coefficient, S, the Nernst coefficient [14], N, and the carrier concentration, n, computed from the Hall coefficient. Unfortunately, the band structure $\epsilon_s(\mathbf{k})$ is not often known because actual samples deviate from the ideal crystal used, for instance, to set up density functional theory (DFT) calculations. Reconciling experimental measurements and electronic structure theory is essential to advance materials discovery. The purpose of m*2t is to enable more realistic comparisons by providing intuitive and high-performance software to simulate transport coefficients from a tunable multi-valley anisotropic band structure model and match the results to experimental measurements of σ, S, and n. Our intent is to further the insight into the band structure of a material solely from electronic transport and to design materials optimization strategies by exploring potential changes of such band structure.

2. Theoretical framework

The study of electronic transport phenomena in crystals requires a model of the stationary dynamics of carriers under electrical and thermal gradients and/or magnetic fields. A common approach involves solving the linearized Boltzmann transport equation to obtain the distribution of charges in the presence of external forces and collision processes within a semi-classical approximation:

$$\frac{\partial f}{\partial \mathbf{r}} \cdot \mathbf{v} + \frac{\partial f}{\partial \mathbf{k}} \cdot \frac{\mathbf{F}}{\hbar} + \frac{\partial f}{\partial t} = \left(\frac{\partial f}{\partial t}\right)_{coll}, \tag{1}$$

where $\mathbf{r}$ is the coordinate vector in real space, $\mathbf{k}$ is the wave vector in the reciprocal space, $f = f(\mathbf{r}, \mathbf{v}, t)$ is the distribution function of charge carriers, $\hbar\mathbf{v} = \partial\epsilon(\mathbf{k})/\partial\mathbf{k}$ is the group velocity, $\mathbf{F} = d(\hbar\mathbf{k})/dt$ is the external force acting on the system of charges. The general assumptions under the Boltzmann transport equation (1) are the following: all the particles are identical and point-like, the fields are assumed classical and reasonably small in magnitude (so that the linear theory is applicable), and the scattering processes are fairly weak to allow for a perturbative approach. These assumptions are usually valid near room temperature and the Boltzmann transport equation is widely used to describe diffusive transport phenomena in solids. The approach breaks down when the geometrical features of the system under investigation have dimensions comparable with the mean free path or the de Broglie wavelength of the particles, for example when modeling nanoscopic electronic devices. In all these situations, the non-equilibrium many-body theory must substitute the semiclassical approach. The essential part of the Boltzmann equation is the collision term in the right-hand side of Eq. (1): it represents the interaction among particles and is responsible for the energy dissipation. A common choice for the collision term assumes that the variation of the charge distribution is linear with the deviations from the equilibrium configuration:

$$\left(\frac{\partial f}{\partial t}\right)_{coll} = -\frac{f - f_0}{\tau}, \tag{2}$$

where f_0 is the Fermi-Dirac distribution of carriers, and $\tau \coloneqq \tau(\mathbf{r}, s, \mathbf{k}, T)$ is the *relaxation-time* for carriers. In the above definition, $\mathbf{r}$ is the position vector, s is the band index, $\mathbf{k}$ is the wave-vector, and T is the temperature. However, in general, the explicit dependence of the relaxation time on the wave vector $\mathbf{k}$ of the first Brillouin zone and s is expressed in terms of the energy eigenvalues $\epsilon_s(\mathbf{k})$. If we assume homogeneity, the relaxation time can be represented as a function of energy and temperature alone, $\tau = \tau(\epsilon_s(\mathbf{k}), T)$, which is the expression that is usually used in practice [15]. Choosing the correct functional form for the relaxation time is crucial to match the experimental measurements. The simplest expression for τ is the *constant relaxation time approximation* (CRTA); it assumes that the scattering between particles is independent of all the variables mentioned above. The CRTA might appear a crude approximation, but it is simple and provides reasonable agreement with experimental data [16]. Important scattering mechanisms for electrons in solids include electron-phonon

scattering and electron-impurity scattering [15], [17], [18], [19]. Many of these mechanisms can be computed from first principles [20] and added in the solution of the Boltzmann transport equation. In the case of multiple interactions occurring in the same system, the total relaxation time τ_T of the carriers is obtained from the Matthiessen's rule:

$$\frac{1}{\tau_T} = \sum_i \frac{1}{\tau_i}. \tag{3}$$

The direct calculations for τ are, however, demanding and often require details of the structure and compositions that are not available.

Following [21], the electrical conductivity σ, the Seebeck coefficient S, and the electron thermal conductivity κ_e take the following form:

$$\sigma = e^2 \mathcal{L}_0, \tag{4a}$$

$$S = -\frac{1}{Te}[\mathcal{L}_0]^{-1} \cdot \mathcal{L}_1, \tag{4b}$$

$$\kappa_e = \frac{1}{T}(\mathcal{L}_2 - \mathcal{L}_1 \cdot [\mathcal{L}_0]^{-1} \cdot \mathcal{L}_1), \tag{4c}$$

where e is the electron charge, and

$$\mathcal{L}_\alpha = \frac{1}{4\pi^3} \int \sum_s \mathbf{v}_s(\mathbf{k})\, \tau(\epsilon_s(\mathbf{k}), T) \cdot \mathbf{v}_s(\mathbf{k})\, (\epsilon_s(\mathbf{k}) - \mu)^\alpha \times \left(-\frac{\partial f_0}{\partial \epsilon} \right) d\mathbf{k}, \tag{5}$$

with $\alpha = 0, 1, 2$ are the *kinetic coefficients*, $\epsilon_s(\mathbf{k})$ is the rigid band structure of the material. Moreover, the carrier density n of a material is usually experimental measured from the Hall effect [22]:

$$n = \frac{1}{ecR_H}, \tag{6}$$

where the Hall tensor R_H is defined as the induced electric field divided by the product of the current density and the applied magnetic field. The standard way to derive a formal expression for the Hall coefficient in the Boltzmann theory of transport involves the magnetic field inside the expression for the Lorentz force, F, and solving Eq. (1) with perturbation theory [14], [23], [24], [25]. Following the formalism of Ref. [25], the electric current is defined in terms of conductivity tensors of different ranks, where each rank is given by the number of external fields the current is coupled to:

$$i_\alpha = \frac{2}{(2\pi)^3} \int \sigma_{\alpha\beta}(\mathbf{k}) \left(-\frac{\partial f_0}{\partial \epsilon} \right) E_\beta d\mathbf{k} + \frac{2}{(2\pi)^3 c} \int \sigma_{\alpha\beta\gamma}(\mathbf{k}) \left(-\frac{\partial f_0}{\partial \epsilon} \right) E_\beta H_\gamma d\mathbf{k}. \tag{7}$$

In the above expression, Einstein's summation convention is used, and E_α and H_α are the electric and magnetic field respectively. The two conductivity tensors $\sigma_{\alpha\beta}$ and $\sigma_{\alpha\beta\gamma}$ are derived from response theory in terms of the group velocity v_α, the 3-dimensional Levi-Civita totally antisymmetric symbol $\epsilon_{\alpha\beta\gamma}$, the inverse of the second-order derivatives of the band structure $M_{\alpha\beta}$, and take the form $\sigma_{\alpha\beta} = e^2 \tau v_\alpha v_\beta$ and $\sigma_{\alpha\beta\gamma} = e^3 \tau^2 \epsilon_{\gamma\delta\rho} v_\alpha v_\delta M^{-1}_{\beta\rho}$. Finally, in this formalism, the Hall 3-rank tensor R_H in Eq. (6) is then obtained as a product of conductivity tensors:

$$R_{\alpha\beta\gamma} = (\sigma^{-1})_{\delta\beta} \cdot \sigma_{\delta\rho\gamma} \cdot (\sigma^{-1})_{\alpha\rho}, \tag{8}$$

and Einstein's summation convention is again used in Eq. (8).

Solving Eqs. (5) and (6) to predict the experimental results requires knowledge of the band structure $\epsilon_s(\mathbf{k})$ and of details of all the scattering processes. This problem is usually solved by assuming the structure and the chemical composition of a compound and by using DFT [26]. If first-principles methods are not viable, choosing the correct functional form for τ requires the formulation of models and, in most cases, a fitting procedure using the experimental data and a specific dependence of τ from the free parameters of the theory (e.g., the Fermi level). The approach presented in this work deviates from this second protocol: instead of assuming knowledge of the microscopic features of a material (in terms of chemical composition, presence and type of impurities, symmetry of the crystal, and scattering mechanisms), we approximate the full density of states (DOS) by a system of second-order expansions around the minima and maxima in the Brillouin zone. Each parabolic expansion represents local phenomena in reciprocal space and is characterized by the effective mass tensor and energy of the critical point. The effective mass is a symmetric matrix defined by six independent values (or equivalently, three principal directions and three principal masses). In this approximation, Eqs. (5) and (6) become numerically tractable and, in some cases, even analytically solvable. Moreover, this approach extends the procedure used to extract experimental values from transport measurements which generally involves fitting an isotropic single parabolic band. By introducing multiple valleys and anisotropy, the code m*2T facilitates indirect measuring procedures of the effective masses of a material from electronic transport, and provides flexible ways to investigate models for the scattering phenomena. It is worth noticing that there are cases in which the band structure is not second-order differentiable, and a more general theory must be used to approximate the full band structure [21]. However, those cases are beyond the goals of the present work.

3. Software design

The software m*2T efficiently computes the transport tensors in Eq. (4) for a generic anisotropic multi-valley parabolic band structure by integrating Eq. (5). The authors are aware that several software are already available in the literature to compute transport coefficients from first-principles band structure calculations. Examples are BoltzTrap [25] and BoltzTrap2 [27], BoltzWann [28], PAOFLOW [29], Phoebe [30]. The first two packages rely on a smoothed Fourier expansion of the band energies to obtain an analytical expression of the band structure. The transport tensors are then obtained by differentiating the band structure and solving the Boltzmann equation. Similarly, BoltzWann solves the Boltzmann equation by computing the band energies and band derivatives using Wannier interpolations. PAOFLOW computes the transport coefficient from the velocity operator obtained by interpolating the band structure using a tight-binding Hamiltonian. Finally, Phoebe is a highly parallel code to solve the Boltzmann equation and compute heat and charge conduction using a scattering matrix formalism based on DFT calculations and Wannier interpolation technique. Differently from these packages, m*2T extracts transport tensors from parabolic band structure models without requiring DFT calculations. The novelty of this code lies in being a high-performance and easy-to-use software to allow experimentalists to compare measurements of the transport coefficients with a more complex model than a single parabolic band, as is commonly done. The software m*2T improves the analysis of the effective masses of materials by using experimental data. Additionally, the code facilitates the designing of the functional form of the relaxation time and opens the way for inverse problem analysis. In other words, m*2T can be used to extract information on the band structure and on the temperature dependence of the relaxation time behind a set of external data of transport coefficients.

The code m*2T has been designed as a hybrid software written in Julia [31] and Python [32] to take advantage of the strengths

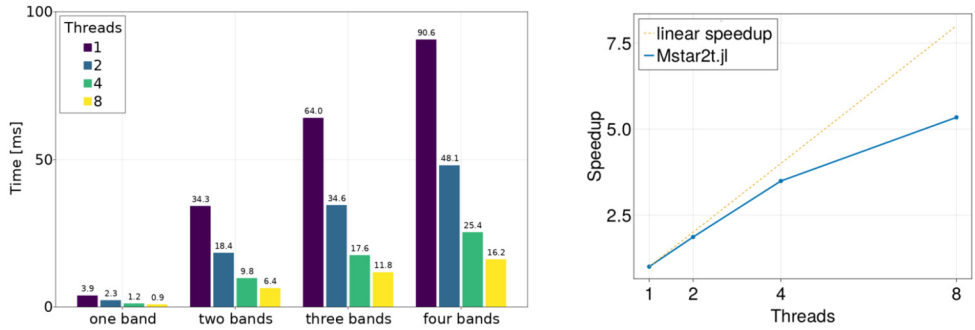

Fig. 1. Wall time of m*2T calculations for band structure models of different complexity and number of threads (left). Speedup plot of the multi-threaded version (right). All tests were performed on a Windows machine with Intel(R) Core(TM) i7-10875H CPU @ 2.30 GHz, 8 Cores, 16 Logical Processors. (For interpretation of the colors in the figure, the reader is referred to the web version of this article.)

of these programming languages. The software is released in two schemes: a Julia package, `Mstar2t.jl`, for the highest performance and a standalone cross-platform application with a graphical user interface (GUI) for a more user-friendly experience. In the first case, the user only needs to import `Mstar2t.jl` in a generic Julia script and then use the methods exposed by the library interface to compute, visualize, and export the results of the simulations. When running the script, it is highly recommended to call the methods inside the Julia REPL to limit the initial compute latency of Julia [33]. Moreover, to boost the performance of the code, the user can run the REPL with multiple threads, and the code will automatically perform all the calculations in parallel (see Fig. 1 for a performance analysis).

The software m*2T can also be run as a standalone software without requiring any knowledge of Julia. To maintain the same performance as the package, the architecture of the software was designed following the client-server paradigm. The code is split into two parts: a computing server and a client interface. The computing unit is written in Julia to take advantage of the high performance in executing linear algebra computations. The main task of this unit is to compute the transport tensors from a single or a set of parabolic band structures. The choice of designing the computing unit as a server overcomes the initial latency of Julia. Once the server is up, the code is designed not to exit as a regular script. Instead, the compiled code keeps running in the background as a service, allowing the user to request other computations and to take full advantage of the performance of a compiled code. The client is a Python interface to set up the parameters of a band structure, request the calculation to the server through a REST API, and plot and export the results. This interface is implemented as a command-line interface (CLI) as well as a GUI. The GUI version of m*2T for Windows is also available as an executable file (.exe). The computing unit is implemented as a web service to listen to client requests on a network connection. We chose to use the representation state transfer (or REST) [34] as the architectural style for the corresponding web API, which defines the communication protocol (HTTP) between the exposed endpoints on the computing server and the Python clients (see Fig. 2). The request of a calculation from the client to the server is sent using an HTTP POST method, and data between the units are exchanged in JSON format. By splitting the code into a computing unit and an interface, the user has the freedom to install the server in any local or remote machine with the desired amount of memory and peak performance while easily sending requests from a separate node, PC, laptop, or even embedded systems. Indeed, the only requirement is an internet connection, the ability to reach the server through the network, and a running Python installation.

The source code of m*2T and the corresponding documentation are available on GitHub on a repository made of two folders, one for the Julia server and the other for the Python interface. Inside

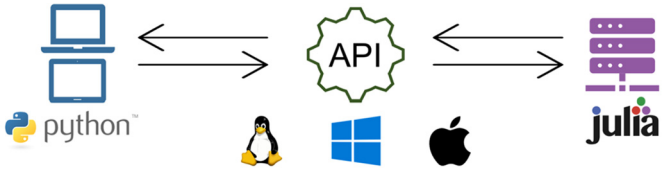

Fig. 2. m*2T client-server architectural model. The server collects the requests from the clients and performs all the operations to compute the transport tensors from a single or a set of parabolic band structures. The server is written in Julia to take advantage of the high performance in executing linear algebra computations. The client is a Python interface to set up the parameters of a band structure, request the calculation to the server through a REST API, plot and export the results. The communication protocol between the endpoints on the computing server and the Python clients is HTTP. (For interpretation of the colors in the figure, the reader is referred to the web version of this article.)

the repository, a `README` file collects the steps to install the code and its dependencies. The two main requirements are a stable Julia installation on the computing machine (version ≥ 1.6) and a Python environment on the interface machine (Python 3).

4. Technical details

The primary purpose of m*2T is the simulation of transport tensors from a set of parabolic band structures in thermodynamic conditions specified by the temperature and the chemical potential. A physical model is defined using a collection of parameters that need to be set up in an input file (for the CLI version, Fig. 3) or through the input window of the GUI (Fig. 4) before running a calculation. There are three main groups of input parameters: *band structure* parameters, *thermodynamic* parameters, and the *relaxation time*. The first group collects the parameters that define each parabolic band: type of band (i.e., $+1$ for a conduction band, -1 for a valence band), effective mass tensor (six real numbers, where the first three are the principal masses and the other three are the Euler principal axes), band energy minimum or maximum, level of degeneracy. The second group of parameters contains the temperature and position of the Fermi level. Finally, the last parameter that has to be specified is the relaxation time τ, which represents the scattering mechanisms between carriers that are included in the system. The functional form for τ can be chosen among already defined expressions (e.g., constant τ, acoustic phonon scattering, and ionic impurities scattering). According to a specific choice of τ, a set of additional parameters is available to adjust its functional form.

For the CLI version, the user must set all the input parameters in an input file that the computing unit reads at the beginning of each calculation. In order to enhance the flexibility of the software, the input file has been designed so that Fermi level, temperature, effective mass components, and energy extrema can be set as a single number or as a range of values. The user can group several computations in a single run and easily explore the behavior

```
# results fullpath
/path/to/output/folder
# export all data [true/false]
false
# number of bands
1
# Fermi level
-0.05:0.02:0.05
# temperature
300:650:10
# bands masses and angles
.5 .5 .5 0.0 0.0 0.0
# band type
1
# energy extrema
0.0
# degeneracy
1
# tau model [constant/acoustic/impurity]
acoustic
# tau acoustic coefficients
ε_min = 0.0
A_sm = 1.0
τm_max = 1.0
T = 250.0
μ_min = 5
μ_max = 5
# tau impurity coefficients
ε_im = 1.0
A_im = 1.0
γ_im = 1.0
```

Fig. 3. Input file template for the transport tensors calculation performed with the command-line interface of m*2T. (For interpretation of the colors in the figure, the reader is referred to the web version of this article.)

of the transport tensors in different regimes. As an example, Fig. 3 reports the input file for a system with a single conduction band with isotropic effective mass and energy minimum at 0.0 eV, temperature between 300 K and 650 K, Fermi level between −0.05 eV and 0.05 eV, and acoustic phonon scattering.

Once the client requests the calculation, the computing unit solves the Boltzmann equation Eq. (1) and obtains the transport tensors by integrating Eq. (4). The following transport tensors are computed: the electrical conductivity σ, Seebeck coefficient S and electrical thermal conductivity κ_e, rank-3 Hall tensor R, Eq. (8), and the value of the carrier concentration n derived from R (Hall effect), Eq. (6). The structure of the computing part is relatively simple. At the higher level, the REST API backend handles the communication with the Python clients. Whenever a computation is requested, the service receives a stream of bytes in JSON format that encodes the parameters of the physical system set up by the user. This information is passed to the `runcalculation` routine that parses all the input parameters, instantiates the Julia data structures, imports or constructs the correct relaxation time functional form, creates the folders structure for the results, and saves the input file for future reference. At the end of these steps, the input data are passed to the `tensor_calculation` routine, which is the actual computing engine of the software. Depending on the requests of the user, the engines calls the functions that compute all the transport tensors. Their names are: `compute_elcond`, `compute_seebeck`, `compute_thermalcond`, `compute_carrierconc`. Moreover, when importing m*2T as a Julia package, the interface exposes five functions to compute the transport coefficients. These functions are: `electrical_conductivity`, `seebeck_coefficient`, `thermal_conductivity`, `hall`, `carrier_concentration`. Finally, the `lorenz_tensor` method can be used to compute the Lorenz tensor in the Wiedemann-Franz law. As described in Section 2, for homogeneous isotropic materials within the relaxation time approximation, the transport properties in Eq. (4) are obtained as a function of three kinetic coefficients $\mathcal{L}_0$, $\mathcal{L}_1$ and $\mathcal{L}_2$. The method `Ln` is at the core of the software that handles the computation of these coefficients by integrating Eq. (5) using the specific relaxation time chosen by the user. By default, the integration of the Boltzmann equation in m*2T is performed numerically by using the Gauss-Laguerre quadrature, a method that is derived from the general Gaussian quadrature rule when the domain of integration is $[0, \infty)$ and the weighting function is of the form e^{-x}. However, it is worth highlighting that fully analytic solutions or combinations of analytic and numerical solutions exist for Eq. (5) for the CRTA and whenever τ is a power function of the energy. Many of these expressions are hard-coded into m*2T so that the integration of the transport tensors turns into function evaluations instead of a call to a numerical integration method, enormously increasing the performance of the software.

Once all the calculations are complete, the code exports the results as a table to a CSV file. This file is named *results.csv* by

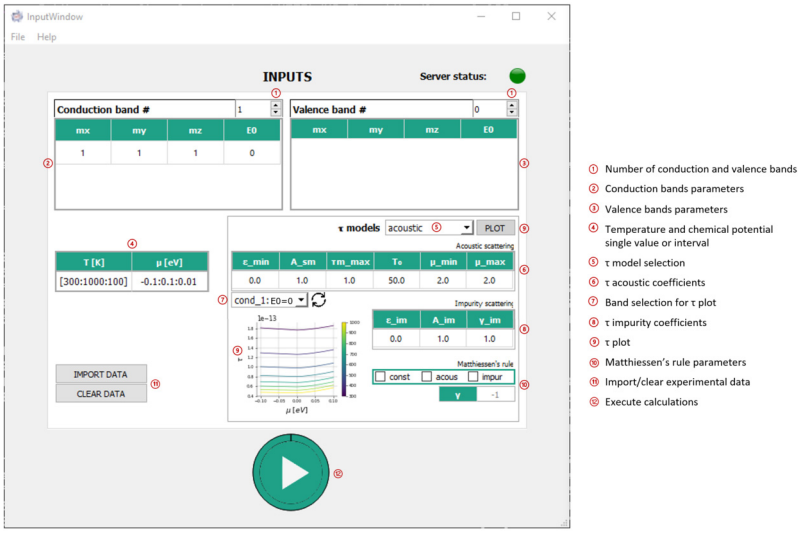

Fig. 4. Input window of the GUI version of the Python interface. This window is used to set up the parameters of the calculation and send the requests of calculations to the computing server. The window is organized with four main boxes: parameters of the conduction bands (top-left), parameters of the valence bands (top-right), temperature and chemical potential (center-left), parameters to define the scattering mechanisms (center-right). Two buttons on the bottom-left corner of the window allow the user to import external data. (For interpretation of the colors in the figure, the reader is referred to the web version of this article.)

	11	22	33	12	13	23
σ	7.66929e+04	7.66929e+04	7.66929e+04	0.00000e+00	0.00000e+00	0.00000e+00
S	-2.83325e-04	-2.83325e-04	-2.83325e-04	-0.00000e+00	-0.00000e+00	-0.00000e+00
K_e	8.71398e-01	8.71398e-01	8.71398e-01	0.00000e+00	0.00000e+00	0.00000e+00
n	-7.76062e+04	-	-	-	-	-

Fig. 5. The output window of the GUI version is provided to visualize and export the results of the computations performed by m*2T. Each graph shows the trend of the electrical conductivity (top-left), the Seebeck coefficient (top-right), the electrical thermal conductivity (bottom-left), and the Hall carrier density (bottom-right) as a function of temperature and chemical potential μ (color bar). The table at the bottom of the window shows each component of the tensors for a chosen pair of temperature and chemical potential. The menu bar at the top of the window can be used to export both plots and data to disk. (For interpretation of the colors in the figure, the reader is referred to the web version of this article.)

default and is located on the path specified by the user in the input file. Every row of the table corresponds to a single band structure model, where each column is a different band parameter, temperature point, and value of the trace of the transport tensor computed at each temperature point. Moreover, a Boolean variable `export_all_data` selects the components to export into separate CSV files. In addition to the computing part, m*2T provides a set of plotting routines to easily visualize the results of the computation. The visualization module of m*2T relies on `Makie.jl` [35] for the Julia package version, and on `Matplotlib` for the Python interface [36].

The GUI can be used as an alternative to the CLI version of the Python interface, which shares the same goals: set up all the parameters of the physical system and request the calculations to the computing unit. We designed the GUI using the PySide library (https://wiki.qt.io/Qt_for_Python), which contains the Python binding of the `C++` Qt framework for GUIs and software applications. Thus, the only prerequisite to run the GUI is a set of dependencies that can be easily installed using a package manager like `pip` or Conda (https://www.anaconda.com/). The `README` file included with m*2T describes all the steps to perform the installation.

Once the GUI is launched, two windows are generated: one is used to enter the parameters of the computation, and the second one to visualize the results (see Figs. 4 and 5). Besides four boxes to set all the parameters of the band structure and the scattering mechanisms, two buttons on the bottom-left corner of the input window allow the user to handle the import of a set of input data. These data are plotted in the output window behind the simulated data. The user can easily compare new simulations with other data (e.g., experimental measurements) and infer the model that best approximates the band structure behind a set of transport measurements. These input data must be collected in a CSV (Comma delimited) *.csv file, or Excel Workbook *.xlsx file and have the form of Table 1. The output window is provided to visualize the results of the computations and to monitor the results before exporting plots and tables into files. Each graph shows the trend of electrical conductivity (top-left), Seebeck coefficient (top-right), electrical thermal conductivity (bottom-left), and Hall carrier density (bottom-right) as a function of temperature T (the chemical potential μ is considered a parameter of the curve). The table at the bottom of the output window reports each component of the tensors for a chosen pair of temperature and chemical potential. Finally, by using the menu bar at the top of the window, the user can easily export both plots and data to disk.

Table 1
Template of the input data table.

Tensor	μ	T_1	T_2	T_3	...	T_n
conductivity	μ_1	$\sigma(\mu_1, T_1)$	$\sigma(\mu_1, T_2)$	$\sigma(\mu_1, T_3)$	...	$\sigma(\mu_1, T_n)$
conductivity	μ_2	$\sigma(\mu_2, T_1)$	$\sigma(\mu_2, T_2)$	$\sigma(\mu_2, T_3)$	...	$\sigma(\mu_2, T_n)$
⋮	⋮	⋮	⋮	⋮	⋮	⋮
conductivity	μ_m	$\sigma(\mu_m, T_1)$	$\sigma(\mu_m, T_2)$	$\sigma(\mu_m, T_3)$	...	$\sigma(\mu_m, T_n)$
seebeck	μ_1	$S(\mu_1, T_1)$	$S(\mu_1, T_2)$	$S(\mu_1, T_3)$	...	$S(\mu_1, T_n)$
⋮	⋮	⋮	⋮	⋮	⋮	⋮
seebeck	μ_m	$S(\mu_m, T_1)$	$S(\mu_m, T_2)$	$S(\mu_m, T_3)$	...	$S(\mu_m, T_n)$
thermal	μ_1	$\kappa(\mu_1, T_1)$	$\kappa(\mu_1, T_2)$	$\kappa(\mu_1, T_3)$	...	$\kappa(\mu_1, T_n)$
⋮	⋮	⋮	⋮	⋮	⋮	⋮
thermal	μ_m	$\kappa(\mu_m, T_1)$	$\kappa(\mu_m, T_2)$	$\kappa(\mu_m, T_3)$	...	$\kappa(\mu_m, T_n)$
concentration	μ_1	$n(\mu_1, T_1)$	$n(\mu_1, T_2)$	$n(\mu_1, T_3)$	...	$n(\mu_1, T_n)$
⋮	⋮	⋮	⋮	⋮	⋮	⋮
concentration	μ_m	$n(\mu_m, T_1)$	$n(\mu_m, T_2)$	$n(\mu_m, T_3)$	...	$n(\mu_m, T_n)$

5. Examples and applications: CRTA

The flexibility of m*2T allows modeling several band structures and doping levels as a function of temperature in seconds. This section collects some illustrative examples assuming the CRTA in the Boltzmann equation, Eq. (1) (in Section 6 the contribution of non-constant scattering time in the transport tensors will be addressed). In each of the following examples, the input file is represented as Julia code that can be trivially transported into the

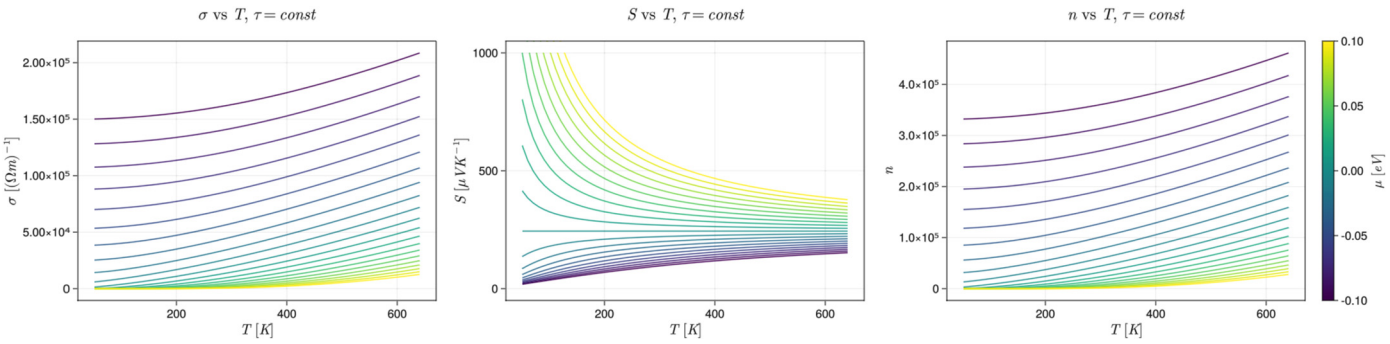

Fig. 6. Transition from an insulating (yellow) to a metallic (purple) regime studied by analyzing the electrical conductivity (left), the Seebeck coefficient (center), and the Hall carrier density (right) as a function of temperature and chemical potential (color bar) for a p-type semiconductor within the CRTA. As discussed in the text, electrical and carrier density increase with temperature in both regimes, while the Seebeck coefficient decreases with temperature in the insulating regime and increases in the metallic regime. Since in both cases the active carriers are positively charged, Seebeck coefficient and Hall charge density are positive. (For interpretation of the colors in the figure, the reader is referred to the web version of this article.)

corresponding CLI input file or GUI input parameters. The figures are obtained using the Julia package `Mstar2t.jl`, but identical plots can be created using the GUI and the standalone software.

5.1. Semiconducting and metallic limits

The case of a single parabolic band has the advantage that a complete analytic expression for electrical and thermal conductivity, Seebeck coefficient and carrier concentration can be derived from the Drude-Sommerfeld model of free electron gas, allowing a direct verification of the consistency of m*2T. To simulate this system, the input parameters are the following:

```
# anisotropic effective mass
mstar = [.1, 1, 10, .0, .0, .0];
# band position
e0 = 0.0;
# band type: valence band
btype = -1;
# single degeneracy
deg = 1;
# chemical potential crossing the band
μ = collect(-.1:0.01:.1);
# temperature
T = collect(50.:10:1000);
# constant relaxation time
τ_form = Scattering.constant();
```

The results (Fig. 6) are in agreement with the analytical expression and numerical simulation in the both metallic and insulator regime for a single parabolic band within the CRTA [21]. The electrical conductivity σ, ($\sigma = \frac{1}{3}Tr(\sigma_{ij})$), increases with temperature for all values of the chemical potential. This effect is due to the broadening of the derivative of the Fermi-Dirac distribution inside the expression for the kinetic coefficients, Eq. (5), which represents that, as the temperature grows, more and more charges are activated and contribute to the electronic transport. The yellow curve displays σ in the insulating regime, in which the value of the chemical potential is above the maximum of the valence band, and therefore the band is fully occupied at $T = 0$. As the chemical potential moves down and enters the valence band, more and more carriers gets activated, and so the electrical conductivity increases in magnitude (darker curves). The behavior of the Hall charge density is identical, in form, to the electrical conductivity, as for a single band electrical conductivity and number of carriers are proportional. The Seebeck coefficient (plot in the center of Fig. 6) is positive, as the carriers that are active in this system are positively charged (which can also be seen by looking at the sign of the Hall carrier density) and raises with temperature in the metallic limit (since the increase in the number of active carriers due to T dominates over the $1/T$ term in Eq. (4)), and decreases with temperature in the insulating regime as the number of active charges saturates when the chemical potential leaves the band. Again, this is in agreement with the analytic expressions [21].

5.2. Bipolar transport

A two-band system with a small band gap may exhibit bipolar transport. This effect on semiconductors has important implications in electronics and photoelectric devices and involves electrons and holes in a crystal at the same time. The input parameters to simulate a system with bipolar transport are the following:

```
# conduction band
# isotropic effective mass
m_1 = [5, 5, 5, .0, .0, .0];
# band position
e0_1 = 1.0;
# conduction band
btype_1 = 1;
# single degeneracy
deg_1 = 1;

# valence band
# anisotropic effective mass
m_2 = [.1, 1, 10, .0, .0, .0];
# band position (moving)
e0_2 = collect(0.0:0.01:1.05);
# valence band
btype_2 = -1;
# single degeneracy
deg_2 = 1;

# Fermi level position
μ = 0.8;
# temperature
T = collect(50.:10:750);
# band gap
gap = e0_1 .- e0_2;
# constant relaxation time
τ_form = Scattering.constant();
```

The band structure is formed by a conduction band with energy minimum equal to `e0_1 = 1.0` eV, and a valence band, that is moving up from `e0_2 = 0.0` eV to `e0_2 = 1.05` eV. Also, the two bands have different effective masses so that they contribute

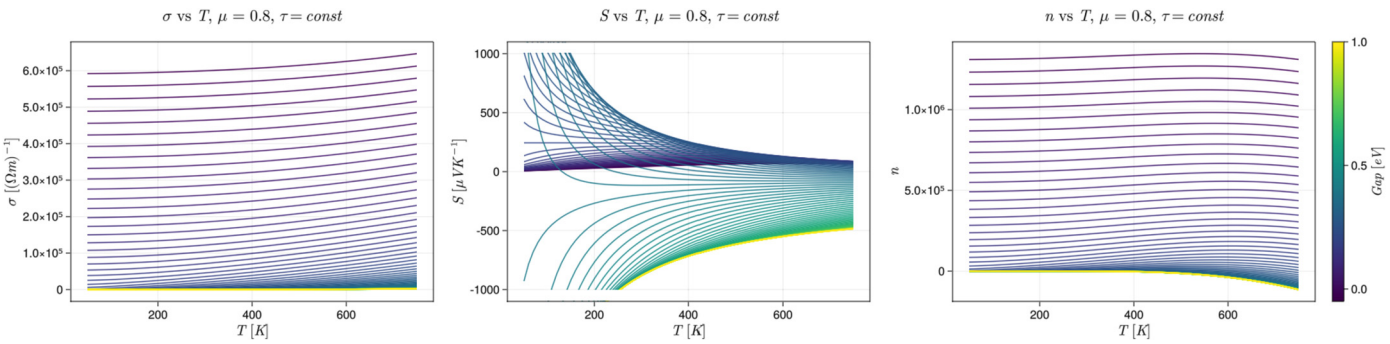

Fig. 7. Effect of bipolar transport on the electrical conductivity (left), the Seebeck coefficient (center), and the Hall carrier density (right) as a function of temperature and band gap (color bar) for a two-band system within the CRTA. The first band is an isotropic conduction band with minimum at `e0_1 = 1.0` eV, the chemical potential is below the conduction band at 0.8 eV, and the second band is an anisotropic valence band with maximum that is moving up from `e0_2 = 0.0` eV to `e0_2 = 1.05` eV, first crossing the chemical potential and then the conduction band. The sign of the Seebeck coefficient and Hall charge density depend on the type of particles that contribute more to the electronic transport. (For interpretation of the colors in the figure, the reader is referred to the web version of this article.)

differently to the transport coefficients. Fig. 7 shows the results of the simulations with `m*2T`, where electrical conductivity, Seebeck coefficient and Hall carrier density are computed as a function of temperature and band gap (color bar) within the CRTA. Electrical conductivity and Hall carrier density are negligible when the band gap is very large, since the chemical potential lies in the gap and both the bands are in the insulating regime. As the band gap closes, more and more charged particles contribute to the electrical current, increasing both the electrical conductivity and the current density. The bipolar transport has an interesting effect on the Seebeck coefficient which is sensitive to the charge sign of the particles that are contributing to the electronic transport. Because of this change of sign, the Seebeck must become zero when there is perfect cancellation between the contributions to the Seebeck of the two bands. In our example, this happens when the band maximum `e0_2` is equal to 0.6 eV, because the chemical potential lies exactly in the middle of the gap. Finally, it is also important to notice that in the proximity of the band edges, while the electrical conductivity and the carrier density drop, the Seebeck coefficient has its maximum (absolute) values.

5.3. Band convergence

This example studies a system with a single conduction band and two valence bands with different energy and effective masses. The focus is on the different contribution to the transport coefficients of the three bands when one of the valence bands converges toward the other one, crossing the chemical potential, and finally entering the insulating regime. The input parameters to simulate this physical system are the following:

```
# conduction band
# isotropic effective mass
m_1 = [1, 1, 1, .0, .0, .0];
# band position
e0_1 = .5;
# conduction band
btype_1 = 1;
# single degeneracy
deg_1 = 1;

# first valence band
# isotropic effective mass
m_2 = [.1, 1, 10, .0, .0, .0];
# band position
e0_2 = 0.0;
# valence band
btype_2 = -1;
# single degeneracy
deg_2 = 1;

# second (moving) valence band
# anisotropic effective mass
m_3 = [.1, 1, 10, .0, .0, .0];
# band position (moving)
e0_3 = collect(-0.5:0.001:0.5);
# valence band
btype_3 = -1;
# single degeneracy
deg_3 = 1;

# Fermi level position
μ = -0.1;
# temperature
T = 500.;
# constant relaxation time
τ_form = Scattering.constant();
```

Fig. 8 shows the electrical conductivity, Seebeck coefficient and Hall carrier density plotted as a function of the distance Δ between the two valence bands. When $\Delta < 0$, the chemical potential crosses both bands. Therefore the electrical conductivity and the carrier density are large while the Seebeck is positive and small. As one of the valence bands moves down, its contribution to the electrical conductivity drops as fewer positive carriers are active in transport while the Seebeck increases. When the band crosses the chemical potential, the electrical conductivity becomes negligible, and the Seebeck has a peak before decreasing again. Again, these results agree with the analytic solutions [16].

5.4. Wiedemann-Franz law

The Wiedemann-Franz law [37] states that the ratio between a metal's electrical and thermal conductivity is linear with the temperature. The justification behind this effect is that in metals, charge and heat carriers are the same free electrons. The coefficient of proportionality is called the Lorentz number L. Analytical predictions for L for a single parabolic model in the constant relaxation time approximation exist in the literature for metallic and insulator regimes [16]. The input parameters to simulate this system are similar to the single parabolic band example:

```
# anisotropic effective mass
m = [.1, 1, 10, .5, 1.6, 5.];
# band position
e0 = 0.0;
```

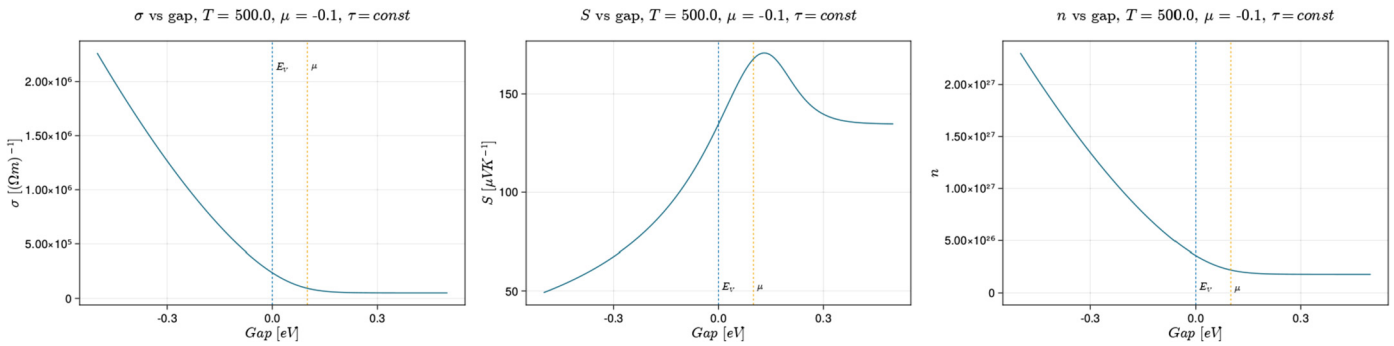

Fig. 8. Effect of band convergence on the electrical conductivity (left), the Seebeck coefficient (center), and the Hall carrier density (right) within CRTA for a system with one isotropic conduction band with minimum at `e0_1 = 0.5` eV, and two anisotropic valence bands, one at `e0_2 = 0.0` eV and the other one moving down from `e0_3 = 0.5` eV to `e0_3 = -0.5` eV. The tensors are plotted as a function of the gap between the two valence bands. The chemical potential is below the fixed valence band at `-0.1` eV. As the valence band moves down, the number of carriers decreases; therefore, the electrical conductivity drops, and the Seebeck coefficient shows a peak. (For interpretation of the colors in the figure, the reader is referred to the web version of this article.)

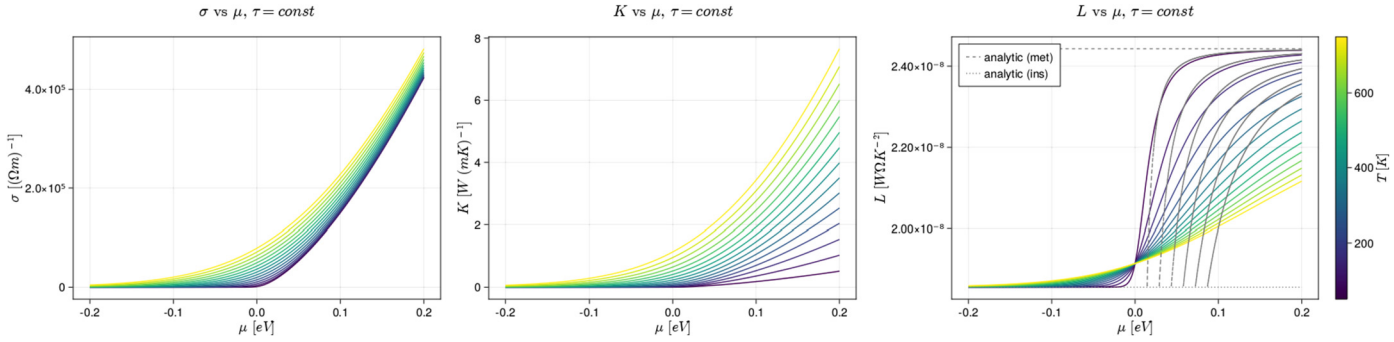

Fig. 9. Wiedemann-Franz law for a single anisotropic conduction band with minimum at `e0 = 0.0` eV. Electrical conductivity (left), thermal conductivity (center), Lorentz number (right) are plotted as a function of the chemical potential and temperature (color bar) within the CRTA. Moving from left to right, the system transitions from insulating regime (far left) to metallic regime (far right). The dotted gray lines in the plot of the Lorentz number (right) show the analytical values obtained within the Drude-Sommerfeld model, which are valid at the metallic and insulating limits [16]. (For interpretation of the colors in the figure, the reader is referred to the web version of this article.)

```
# conduction band
btype = 1;
# single degeneracy
deg = 1;
# transition between metallic
# and insulting regime
μ = collect(-0.2:0.0005:0.2);

# temperature
T = collect(50.:50:750);
# constant relaxation time
τ_form = Scattering.constant();
```

Fig. 9 shows the plots for the electrical and thermal conductivity, and Lorenz number as a function of chemical potential and temperature (color bar) for a single conduction band with minimum at 0.0 eV. In particular, in the far left part of the plots, the chemical potential is below the band minimum and therefore the system is in the insulating regime. On the other hand, in the far right part of the graphs, the chemical potential is equal to 0.2 eV and so it is inside the conduction band; therefore the system behaves as a metal. Also, the dotted gray lines in the plot of the Lorentz number represent the analytic values computed from the single parabolic model in the metallic and insulating limits. As can be seen, the simulations obtained with m*2T are in agreement with the accepted theoretical values [16].

6. Examples and applications: non-constant τ models

Although widely used, the CRTA does not capture the behavior of the transport coefficients as function of temperature. For instance, experimental measurements of the electrical conductivity show that σ increases when heating the sample for a semiconductor and decreases with temperature for a metal. The transport coefficients are also sensitive to the doping level, and to the nature and quantities of impurities in a material. In order to reproduce physical phenomena, a temperature dependence of the relaxation time $\tau(T)$ must be accounted for. The temperature dependence of τ can simulate different transport regimes that may be related to the specific scattering phenomena or the relative weight they may have at different temperatures. Two important scattering mechanisms are included in m*2T: the acoustic phonon scattering, and the ionized impurity scattering. The acoustic phonon scattering, τ_{ac}, describes the interaction between electrons and thermal vibrations, and explains the change of behavior of the electrical conductivity between a metal and a semiconductor. In contrast, τ_{im} allows a description of the change in the transport coefficients due to the presence of impurities and imperfections.

Following [23], the relaxation time for the acoustic phonon scattering is inversely proportional to temperature, and the dependence on the energy changes according to the position of the chemical potential with respect to the extremum of the band:

$$\tau_{ac}(T,\mu) = \begin{cases} \dfrac{A_{sm}}{\sqrt{\mu-\epsilon_{sm}}} \cdot \dfrac{1}{T-T_0} & \text{if } \mu < \epsilon_0 \\ \dfrac{A_m(\mu-\epsilon_0)^{3/2}+B_m}{T-T_0} & \text{if } \mu > \epsilon_0. \end{cases} \tag{9}$$

In m*2T the two functions are smoothly joined with a sigmoid function. The essential part of Eq. (9) is the dependence on temperature ($\tau \sim 1/T$) and chemical potential ($\tau \sim 1/\sqrt{\mu}$ or $\tau \sim \mu^{3/2}$). The parameters ϵ_0, ϵ_{sm}, T_0, A_{sm}, A_m, and B_m can be tuned

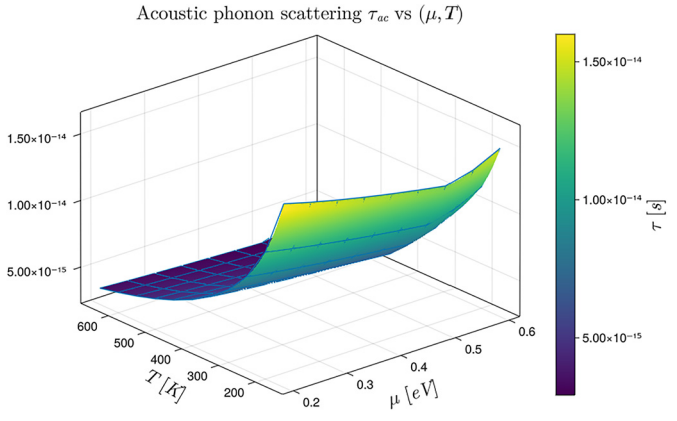

Fig. 10. Functional form for the acoustic phonon scattering τ_{ac} in Eq. (9) as a function of temperature and chemical potential. The relaxation time drops with temperature ($\tau \sim 1/T$) for both semiconducting and metallic regimes, and decreases (increases) with the chemical potential in the semiconducting (metallic) regime. (For interpretation of the colors in the figure, the reader is referred to the web version of this article.)

to match the experimental data. We notice that a direct calculation of these parameters it is very demanding for real materials and beyond the scope of learning from experiments. The parameter ϵ_0 is the critical point of the band in eV, ϵ_{sm} is the value of the energy at which the relaxation time diverges (no scattering) or, similarly, the first point in energy at which τ_{ac} is computed. Since energy is always defined as difference from a common reference, we chose to set this reference as the energy of the lowest band (called ϵ_{min}, in eV). Therefore, ϵ_{sm} is defined as a distance from ϵ_{min}, $\epsilon_{sm} = \epsilon_{min} - \mu_{min}$ using the μ_{min} input parameter of the interface of m*2T. The parameter A_{sm} is a multiplicative constant in front of the functional expression of τ_{ac} for semiconductors in units of $5 \cdot 10^{-20} s$. T_0 is the minimum temperature at which τ_{ac} is defined and can be used to control the temperature at which τ_{ac} diverges. Finally, the function in Eq. (9) has two more degrees of freedom, A_m and B_m. One of them is fixed by imposing the continuity between the two pieces of the expression, while the second one is modified through τ_{max} (in eV), which is the parameter that sets the maximum value of the second form of τ_{ac}: $\tau_{ac}(\epsilon_0 + \mu_{max}) = \tau_{max}$, in units of $2 \cdot 10^{-12} s$. An example of the functional form for the acoustic phonon scattering implemented in m*2T can be seen in Fig. 10.Figs. 11 and 12 show the prediction of m*2T for the electrical conductivity, Seebeck coefficient, and Hall carrier density for a single conduction band when acoustic phonon scatterings are included. These results should be compared with the ones obtained within the CRTA, as in Fig. 6. When the electron-phonon interaction is present, the scattering rate increases with temperature, so the relaxation time becomes smaller. In a semiconductor, the number of carriers is small compared to that in a metal and grows considerably with temperature. Since this effect dominates over the decrease of τ due to electron-phonon scattering, the electrical conductivity increases with temperature. In a metal, there are more carriers from the start, the increase in carrier density due to temperature becomes lower than in the semiconducting regime, and the scattering rate dominates over the increment of n. Therefore, the electrical conductivity changes behavior, and it decreases with temperature due to acoustic phonons (see the crossover of the parametric curves in the first plot of Fig. 12 when the Fermi level crosses the minimum of the conduction band). The code to simulate this effect with m*2T is identical to one for the CRTA; the only change is in the last line, where `τ_form = Scattering.acoustic();` is used instead of `τ_form = Scattering.constant();`.

A more complex example is a system of two valence and two conduction bands with a gap. Even in this case, the balance between the effect of acoustic phonons and the increase in temperature of the carrier concentration determines a departure from the behavior of the electrical conductivity predicted within the CRTA, as can be seen in Fig. 13. The m*2T input file for this system is:

```
# conduction band #1
m_1 = [.8, .8, .8, 0.0, 0.0, 0.0];
e0_1 = .5;
type_1 = 1;
# conduction band #2
m_2 = [.5, .5, .5, 0.0, 0.0, 0.0];
e0_2 = .35;
type_2 = 1;
# valence band #1
m_3 = [1., 1., 1., 0.0, 0.0, 0.0];
e0_3 = .32;
type_3 = -1;
# valence band #2
m_4 = [.7, .7, .7, 0.0, 0.0, 0.0];
e0_4 = .25;
type_4 = -1;

μ = collect(.2:0.01:.6);
T = collect(150:50:650);
τ_form = Scattering.acoustic();
```

In all these calculations, we assumed that the majority of the electrons that are active in transport and can be scattered are the ones with energy $\epsilon \sim \mu \pm \Delta E$, with $\Delta E \sim k_B T$. Thanks to this physical condition, the integration of Eq. (5) is extremely efficient because

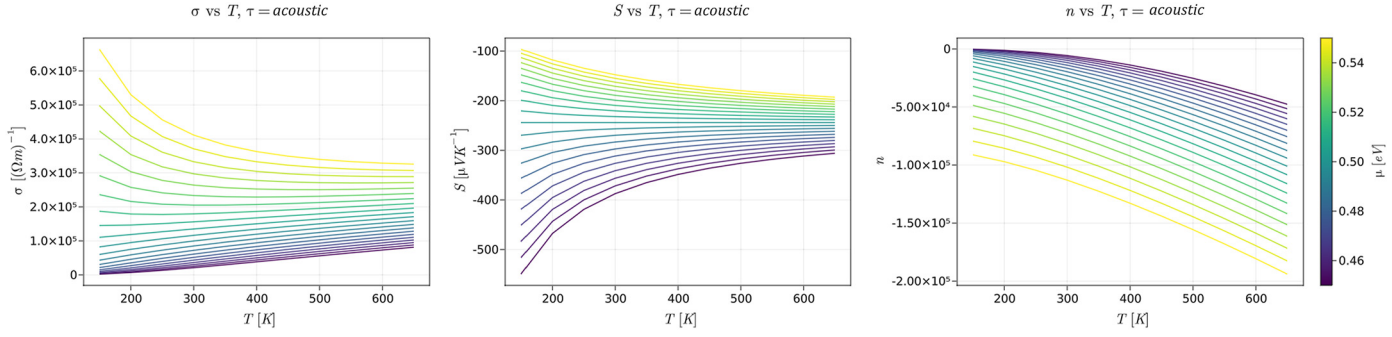

Fig. 11. Electrical conductivity (left), Seebeck coefficient (center), and Hall carrier density (right) as a function of temperature and chemical potential (color bar) for a single band n-type semiconductor transitioning from insulating (purple) to the metallic (yellow) regime with acoustic phonons scattering τ_{ac}. (For interpretation of the colors in the figure, the reader is referred to the web version of this article.)

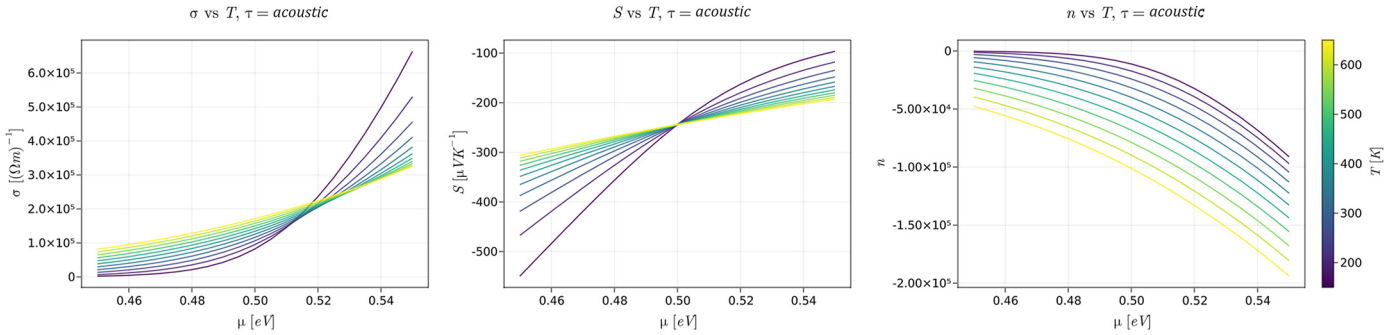

Fig. 12. Effect of acoustic phonon scattering on the electrical conductivity (left), the Seebeck coefficient (center), and the Hall carrier density (right) as a function of chemical potential and temperature (color bar) for a single band n-type semiconductor transitioning from insulating (purple) to the metallic (yellow) regime. Differently from the CRTA, Fig. 6, the electrical conductivity decreases with temperature in the metallic regime due to the interaction between electrons and acoustic phonons. This change of behavior is illustrated by the crossover of the bundle of lines at constant temperature in the first plot. (For interpretation of the colors in the figure, the reader is referred to the web version of this article.)

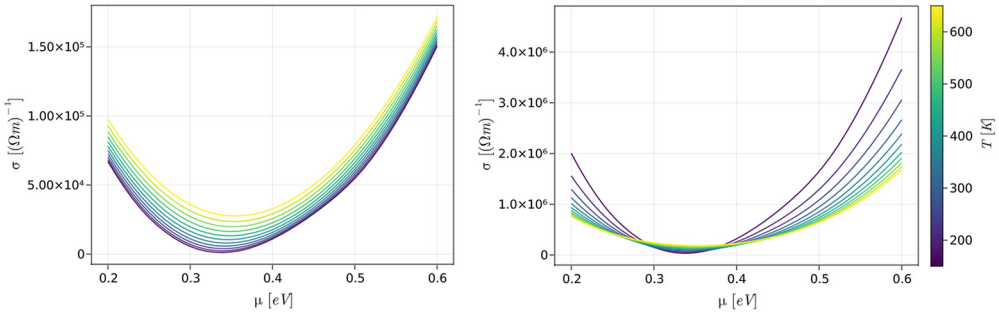

Fig. 13. Electrical conductivity as a function of chemical potential and temperature within CRTA (left), and with acoustic phonon scattering (right), for a four-band system with two valence bands (maxima at `e0_1 = -0.32` eV and `e0_1 = -0.25` eV) and two conduction bands (minima at `e0_3 = 0.35` eV and `e0_4 = 0.5` eV), and with a gap of `0.03` eV. The chemical potential ranges from `0.2` eV to `0.6` eV and the temperature from 150 K (purple) to 650 K (yellow). The plot on the right shows the change of temperature dependence of the electrical conductivity due to the presence of acoustic phonons: it decreases with temperature in the metallic regime (left and right side of the right plot), and it increases with temperature when the chemical potential is within the gap and the system behaves like a semiconductor. (For interpretation of the colors in the figure, the reader is referred to the web version of this article.)

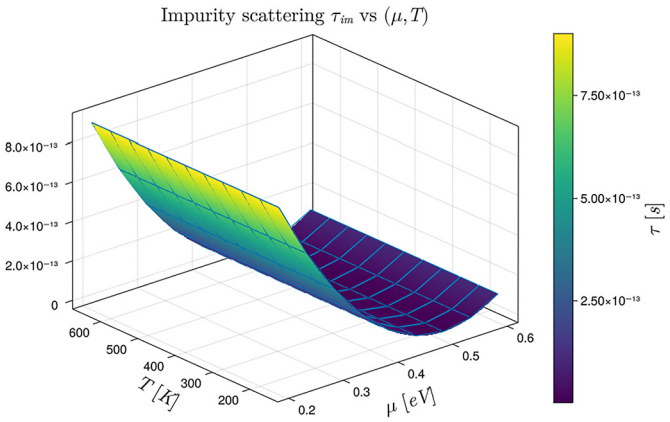

Fig. 14. Functional form for the impurity scattering τ_{im} in Eq. (10) as a function of temperature and chemical potential. The relaxation time is constant with temperature, inversely proportional to density of impurities, and drops when the chemical potential matches the energy of the impurity ϵ_{im}. (For interpretation of the colors in the figure, the reader is referred to the web version of this article.)

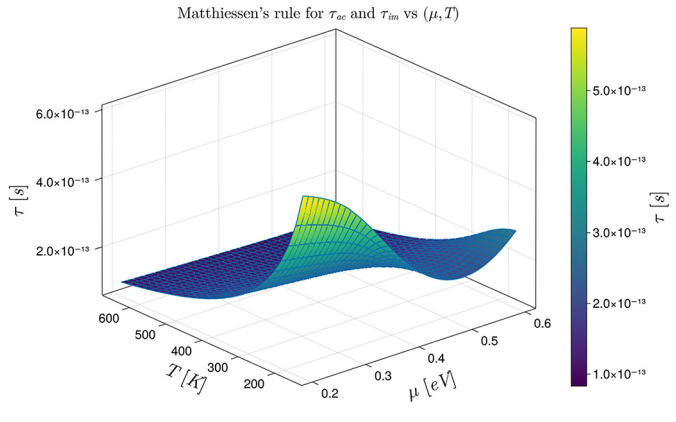

Fig. 15. Functional form for the relaxation time obtained by applying Matthiessen's rule, Eq. (3) to the acoustic phonon scattering τ_{ac} and the impurity scattering τ_{im}, as a function of temperature and chemical potential. (For interpretation of the colors in the figure, the reader is referred to the web version of this article.)

τ comes out of the integral allowing for the evaluation of Eq. (5) with analytical expressions.

There is a second built-in functional form for the relaxation time in m*2T, the one for the impurity scattering:

$$\tau_{im} = \left[\frac{A_{im}\gamma^2}{(\mu - \epsilon_{im})^2 + \gamma^2} \right]^{-1} . \tag{10}$$

The impurity scattering rate (relaxation time) is constant with temperature [38] and has a peak (minimum) with value A_{im} $(1/A_{im})$ when the chemical potential matches the energy of the impurity ϵ_{im}. The parameter A_{im} is in units of $10^{13} s^{-1}$ and is proportional to the density of impurities ($A_{im} \sim n_{im}$), while γ is related to the dispersion of the curve, see Fig. 14. Analyzing systems with a single scattering process can be useful for theoretical inquiry, particularly when restricting the study to specific temperature and chemical potential regimes. However, the scenario is more complicated when dealing with actual materials. For instance, for a system with impurities and in which the current is limited by acoustic phonons, the two effects must be included together. In m*2T the two effects are automatically summed up

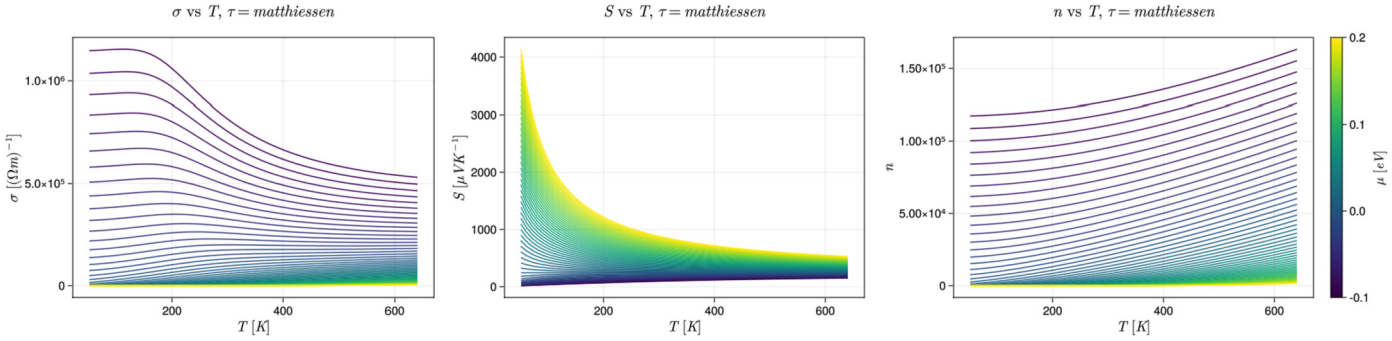

Fig. 16. Electrical conductivity (left), Seebeck coefficient (center), and Hall carrier density (right) as a function of temperature and chemical potential (color bar) for a single band p-type semiconductor with energy minimum at 0.0 eV transitioning from metallic (purple) to the insulating (yellow) regime. The relaxation time is obtained by applying Matthiessen's rule, Eq. (3) to the acoustic phonon scattering τ_{ac}, Eq. (9), and the impurity scattering τ_{im}, Eq. (10). Since the latter dominates at low temperature, the electrical conductivity remains almost constant in the first part of the left plot. As the temperature increases, the density of phonons grows very rapidly and the acoustic phonon scattering takes over the impurity scattering and becomes the primary source of dissipation. Therefore, the electrical conductivity recovers the behavior seen in Fig. 11. (For interpretation of the colors in the figure, the reader is referred to the web version of this article.)

using Matthiessen's rule, Eq. (3), and the resulting relaxation time is shown in Fig. 15. Interestingly, since τ_{im} is constant in temperature while τ_{ac} rapidly increases with temperature, when studying the effect of these two scatterings to the transport properties of a material as a function of temperature, there exists a temperature scale $\bar{T}$ at which the acoustic phonon scattering takes over the impurity scattering. Around this critical point, the behavior of the electrical conductivity, for instance, changes considerably. At low temperature, τ_{im} is the primary source of scattering for the electrical charges. In this temperature regime, the electrical conductivity increases with temperature and is inversely proportional to the density of impurities and magnitude of the coupling between them and the electrical current. On the other hand, as the temperature increases, so does the phonon density, and more and more acoustic phonons are coupled to the carriers. As discussed above, when the temperature matches $\bar{T}$, the electrical conductivity changes its temperature dependence, it stops increasing with T and starts decreasing, see Fig. 16.

7. Conclusions

The software m*2t is a new user-friendly, high-performance tool to study electronic transport coefficients from a generic multi-valley anisotropic band structure model. To aid the interpretation of experiments and the quantification of the effective masses, m*2t efficiently compute the electrical conductivity, the Seebeck coefficient, the electron thermal conductivity, and the carrier concentration within the Boltzmann transport theory. Examples were provided to show the usage and features of m*2t. The first group of examples focuses on the constant relaxation time approximation. In the second group of examples, m*2t was used to recover the correct temperature dependence of the electrical conductivity for a semiconductor transitioning from insulating to the metallic regime due to acoustic phonon scattering and to study the behavior of the transport coefficients for a semiconductor with impurities. To facilitate the comparison between simulations and experimental measurements, we provide a GUI to visualize the results of the calculations together with imported experimental data. By tuning the parameters of the parabolic models and choosing the correct scattering mechanisms, m*2t provides a method to estimate the effective masses that characterize the underlying band structure of the material under study. We are currently considering to automate the reconstruction of the band structure model by solving the inverse problem of predicting effective masses directly from measurements of transport coefficients.

Declaration of competing interest

The authors declare that they have no known competing financial interests or personal relationships that could have appeared to influence the work reported in this paper.

Data availability

The code will be available after publication on the following GitHub repository: https://github.com/marcofornari/etransport.git.

Acknowledgements

The authors are greateful to Troy Lyons, Virginia Carnevali, Andrew Supka, Lorenzo Resca for helpful discussions regarding the theoretical foundation and the computational implementation of the software. The code has been inspired and motivated by the authors' collaboration with experimentalists Paz Vaqueiro, Emmanuel Guilmeau, and Kaya Wei.

This work is based on or developed under this contract, stated in the following terms: "This material is based upon work supported by the Defense Advanced Research Projects Agency (DARPA) under Contract No. HR001122C0063. Any opinions, findings and conclusions or recommendations expressed in this material are those of the authors and do not necessarily reflect the views of DARPA."

References

[1] H. Hasegawa, Phys. Rev. 129 (3) (1963) 1029–1040, https://doi.org/10.1103/PhysRev.129.1029, publisher: American Physical Society, https://link.aps.org/doi/10.1103/PhysRev.129.1029.

[2] J.M. Luttinger, Phys. Rev. 102 (4) (1956) 1030–1041, https://doi.org/10.1103/PhysRev.102.1030, https://link.aps.org/doi/10.1103/PhysRev.102.1030.

[3] J.C. Hensel, G. Feher, Phys. Rev. 129 (3) (1963) 1041–1062, https://doi.org/10.1103/PhysRev.129.1041, https://link.aps.org/doi/10.1103/PhysRev.129.1041.

[4] L. Eaves, R.A. Hoult, R.A. Stradling, R.J. Tidey, J.C. Portal, S. Askenazy, J. Phys. C, Solid State Phys. 8 (7) (1975) 1034–1053, https://doi.org/10.1088/0022-3719/8/7/019, https://iopscience.iop.org/article/10.1088/0022-3719/8/7/019.

[5] R.J. Nicholas, J.C. Portal, C. Houlbert, P. Perrier, T.P. Pearsall, Appl. Phys. Lett. 34 (8) (1979) 492–494, https://doi.org/10.1063/1.90860, http://aip.scitation.org/doi/10.1063/1.90860.

[6] P.G. Harper, J.W. Hodby, R.A. Stradling, Rep. Prog. Phys. 36 (1) (1973) 1, https://doi.org/10.1088/0034-4885/36/1/001, https://dx.doi.org/10.1088/0034-4885/36/1/001.

[7] C.K. Sarkar, R.J. Nicholas, J.C. Portal, M. Razeghi, J. Chevrier, J. Massies, J. Phys. C, Solid State Phys. 18 (13) (1985) 2667–2676, https://doi.org/10.1088/0022-3719/18/13/013, https://iopscience.iop.org/article/10.1088/0022-3719/18/13/013.

[8] A. Damascelli, Phys. Scr. T 109 (2004) 61, https://doi.org/10.1238/Physica.Topical.109a00061, https://iopscience.iop.org/article/10.1238/Physica.Topical.109a00061.

[9] W.G. Spitzer, H.Y. Fan, Phys. Rev. 106 (5) (1957) 882–890, https://doi.org/10.1103/PhysRev.106.882, publisher: American Physical Society, https://link.aps.org/doi/10.1103/PhysRev.106.882.
[10] D.L. Young, T.J. Coutts, V.I. Kaydanov, A.S. Gilmore, W.P. Mulligan, J. Vac. Sci. Technol., A 18 (6) (2000) 2978–2985, https://doi.org/10.1116/1.1290372, publisher: American Vacuum Society, https://avs.scitation.org/doi/10.1116/1.1290372.
[11] X. Bao, T. Schlesinger, R. James, in: T. Schlesinger, R.B. James (Eds.), Semiconductors and Semimetals, in: Semiconductors and Semimetals, vol. 43, Elsevier, 1995, pp. 111–168, https://www.sciencedirect.com/science/article/pii/S008087840862743X.
[12] L.D. Landau, Zh. Eksp. Teor. Fiz. 30 (6) (1956) 1058.
[13] A. Supka, N.A. Mecholsky, M. Buongiorno Nardelli, S. Curtarolo, M. Fornari, Engineering 10 (2022) 74–80, https://doi.org/10.1016/j.eng.2021.03.031.
[14] M. Zebarjadi, S.E. Rezaei, M.S. Akhanda, K. Esfarjani, Phys. Rev. B 103 (14) (2021) 144404, https://doi.org/10.1103/PhysRevB.103.144404, publisher: American Physical Society https://link.aps.org/doi/10.1103/PhysRevB.103.144404.
[15] C. Jacoboni, Theory of electron transport in semiconductors, 2010.
[16] N.A. Mecholsky, R. Al Rahal Al Orabi, M. Fornari, in: Inorganic Thermoelectric Materials: From Fundamental Concepts to Materials Design, The Royal Society of Chemistry, 2021, https://doi.org/10.1039/9781788019590-00053.
[17] S. Datta, Quantum Transport: Atom to Transistor, Cambridge University Press, 2005.
[18] M. Lundstrom, Fundamentals of Carrier Transport, 2nd edition, Cambridge University Press, 2000.
[19] D. Ferry, S.M. Goodnick, Transport in Nanostructures, Cambridge Studies in Semiconductor Physics and Microelectronic Engineering, Cambridge University Press, 1997.
[20] S. Poncé, E.R. Margine, C. Verdi, F. Giustino, Comput. Phys. Commun. 209 (2016) 116–133, https://doi.org/10.1016/j.cpc.2016.07.028, https://www.sciencedirect.com/science/article/pii/S0010465516302260.
[21] N.A. Mecholsky, L. Resca, I.L. Pegg, M. Fornari, Phys. Rev. B 89 (15) (2014), https://doi.org/10.1103/PhysRevB.89.155131.
[22] E.H. Hall, Am. J. Math. 2 (3) (1879) 287–292, https://doi.org/10.2307/2369245, publisher: Johns Hopkins University Press, http://www.jstor.org/stable/2369245.
[23] A.H. Wilson, The Theory of Metals / A.H. Wilson, 2nd edition, Cambridge Uni. Press, Cambridge, England, 1953.
[24] J.M. Ziman, Principles of the Theory of Solids, 2nd edition, Cambridge University Press, 1972.
[25] G.K.H. Madsen, D.J. Singh BoltzTraP, Comput. Phys. Commun. 175 (1) (2006) 67–71, https://doi.org/10.1016/j.cpc.2006.03.007.
[26] R.M. Martin, Electronic Structure: Basic Theory and Practical Methods, Cambridge University Press, 2004.
[27] G.K.H. Madsen, J. Carrete, M.J. Verstraete, Comput. Phys. Commun. 231 (2018) 140–145.
[28] G. Pizzi, D. Volja, B. Kozinsky, M. Fornari, N. Marzari, Comput. Phys. Commun. 185 (1) (2014) 422–429.
[29] F.T. Cerasoli, A.R. Supka, A. Jayaraj, M. Costa, I. Siloi, J. Sławińska, S. Curtarolo, M. Fornari, D. Ceresoli, M. Buongiorno Nardelli, Comput. Mater. Sci. 200 (2021).
[30] A. Cepellotti, J. Coulter, A. Johansson, N.S. Fedorova, B. Kozinsky, J. Phys. Mater. 5 (3) (2022).
[31] J. Bezanson, A. Edelman, S. Karpinski, V.B. Shah Julia, SIAM Rev. 59 (1) (2017) 65–98, https://doi.org/10.1137/141000671, publisher: Society for Industrial and Applied Mathematics, https://epubs.siam.org/doi/abs/10.1137/141000671.
[32] G. van Rossum, Python, https://www.python.org/.
[33] T. Holy, J. Bezanson, J. Nash, Analyzing sources of compiler latency in Julia: method invalidations, https://julialang.org/blog/2020/08/invalidations/.
[34] R.T. Fielding, Architectural Styles and the Design of Network-based Software Architectures, Doctoral dissertation, University of California, Irvine, 2000.
[35] S. Danisch, J. Krumbiegel, J. Open Sour. Softw. 6 (65) (2021) 3349, https://doi.org/10.21105/joss.03349.
[36] J.D. Hunter, Comput. Sci. Eng. 9 (3) (2007) 90–95, https://doi.org/10.1109/MCSE.2007.55.
[37] R. Franz, G. Wiedemann, Ann. Phys. 165 (8) (1853) 497–531, https://doi.org/10.1002/andp.18531650802, _eprint, https://onlinelibrary.wiley.com/doi/pdf/10.1002/andp.18531650802.
[38] A. Lavasani, D. Bulmash, S. Das Sarma, Phys. Rev. B 99 (8) (2019) 085104, https://doi.org/10.1103/PhysRevB.99.085104, publisher: American Physical Society, https://link.aps.org/doi/10.1103/PhysRevB.99.085104.